Supplementary Information

Easily Available 3D Flow Fields through 3D-Patterned GDL to Enhanced PEMFC Performance by Excellent Water-Gas Separated Transport

Xi Cheng,[a,b] Can He,[b] Qinglin Wen,[b] Yuzhuo Jiang,[b] Wei Li,[b] Jiahao Huang,[a,b] Wentao Huang,[b] Xingyu Zhu,[b] Xueyan Chu,[b] Fandi Ning,[b] Lining Sun,[a] Bin Tian,[b] Xiaochun Zhou*[b,c]

a. Department of Chemistry, College of Sciences, Shanghai University, Shanghai, 200444, China
b. Advanced Materials Division, Suzhou Institute of Nano-Tech and Nano-Bionics, Chinese Academy of Sciences (CAS), Suzhou, 215123, China
c. Key Laboratory of Precision and Intelligent Chemistry, University of Science and Technology of China, Hefei, 230026, China

Email: xczhou2013@sinano.ac.cn

CONTENT

SI-1 Materials and Characterizations

1. Materials

The chemicals for preparing the 3D-patterned gas diffusion layers (GDL) were as follows: single-walled carbon nanotubes (SWCNT, OCSiAl Tuball^{TM}, 80wt%), multi-walled carbon nanotubes (MWCNT, Shandong Dazhan Nanomaterials, 95wt%), short carbon fiber (CF, ~150 μm, Toray, Co., Ltd.), polytetrafluoroethylene (PTFE, Sigma-Aldrich Co., Ltd.), sodium dodecyl benzene sulfonate (SDBS, Tianjin BASF chemical, Co., Ltd.). Octadecyl trichlorosilane, methanol, and toluene were purchased from Sinopharm Chemical Reagent Co., Ltd, China. The conventional GDLs (SGL 28BC) were purchased from Sigracet®, polytetrafluoroethylene (PTFE, Sigma-Aldrich Co., Ltd.). All chemicals were obtained conventionally and used without further purification unless specified.

2. Physical characterizations of GDL and 3D flow field

The overall shape of GDL and water management visual observation were recorded by the camera. The morphology and structure of GDL were characterized by scanning electron microscope (Nova NanoSEM450, FEI Company, USA). The contact angle images were recorded by contact angle measuring device (Sindin SDC-200S, Kunshan Shengding Industrial Intelligent Technology Co.,Ltd.,China) (SINDIN SDC-200s) with a high-speed camera of Dahang. The electrical conductivity was tested via multifunctional digital four-probe tester (ST-2258C, Suzhou Jingge Electronic Co.,Ltd.,China). The gas permeability was tested according to the previous reports.[1]

3. Preparation of the 3D-patterned GDL

Preparation of SWCNT and MWCNT dispersion. The SWCNTs and MWCNTs, with SDBS (mass ratio CNT: SDBS = 1:15), were placed in ultrapure water and sonicated for 3 hours at the concentration of 2 mg mL^{-1} by ultrasonic cell grinder, respectively.

Preparation of CF dispersion. The CFs, with SDBS (mass ratio CNT: SDBS = 1:10), were placed in ultrapure water and sonicated for 10 min at the concentration of 10 mg mL^{-1} by ultrasonic cleaner.

Design and preparation of mold. The mold was designed by modeling software UG NX12.0 and was printed by the BlueMaker 3D printer (BlueMaker Co., Ltd.). The raw material was white resin.

Preparation of GDL. The preparation process can be divided into four steps. First, SWCNTs, MWCNTs, CFs, and PTFE (mass ratio of 1:7:0:2.67, total mass loading of 1.067 mg cm^{-2}) were mixed evenly and then filtrated on the mixed cellulose esters (MCE) filter membrane to form the microporous layer (MPL). Second, SWCNTs, MWCNTs, CFs, and PTFE (mass ratio of 2.5:17.5:1:7.5, total mass loading of 3.75 mg cm^{-2}) were mixed evenly and then filtrated on the MPL to form the support layer. Thirdly, SWCNTs, MWCNTs, CFs, and PTFE (mass ratio of 1:9:6:4, total mass loading of 6 mg cm^{-2}) were mixed evenly and then filtrated with the mold on the support layer to form the 3D-patterned layer. After draining the water, we removed the mold and then uncovered the MCE membrane after drying in the oven. Finally, the 3D-patterned GDL was placed in the muffle furnace at 350℃ for 30 minutes to remove the remained SDBS and increase its strength.

4. Preparation of MEA

The membrane electrode assembly (MEA) included the following components: the 3D-patterned GDL as the cathode, SGL 28BC as the anode, and catalyst-coated membrane (CCM). CCM was purchased from Suzhou Sinero Technology Co., Ltd (China). The proton exchange membrane (PEM) of CCM is Gore M820.15 (12 μm). The catalyst of this CCM is JM Hispec 9100 (55.5-58.5%), and the anode and cathode Pt loadings are 0.12 and 0.48 mg cm^{-2}, respectively. The active area of MEA was 3*5 cm^2.

The fuel cell operates at a compression pressure of 1 MPa, regulated with a torque wrench to ensure the uniform force distribution across the MEA. The calculated tightening torque is 1.5 N·m and it is maintained constant in subsequent experiments. The GDL was compressed by 40%.

5. Flow Field Information

In the fuel cell, we used a waveform bipolar plate in the cathode and a parallel bipolar plate in the anode. Both the channel width and rib width of the two flow fields were 1 mm. The flow channel depth is 200 μm.

6. The fuel cell tests

The fuel cell performance was tested with Toyo Fuel Cell Test System equipped with 890e Fuel Cell Test Loads (Scribner Associates Inc.) and 885-HS Fuel Cell Potentiostat (Scribner Associates Inc.).

Polarization curves. The curves were recorded under the conditions of 80 ºC, 100 kPa_{gauge} back pressure, and 60%RH for both anode and cathode under hydrogen-air conditions. The hydrogen stoichiometric ratio was 1.5. The air stoichiometric ratio changed among 1.5, 2.0, and 2.5. The minimum air flow rate was 0.5 NL min^{-1} and the minimum H_2 flow rate was 0.3 NL min^{-1}, respectively.

Electrochemical impedance spectroscopy (EIS) test. The test conditions of EIS were the same as those of polarization curves. The EIS was tested at the sweep frequency mode at the potential of

0.6 V. The frequency range of EIS test was 10 kHz-0.1 Hz. The amplitude of AC signal was kept at 10% of DC current. The impedance data was modeled and fitted using ZView2 software.

7. Hydrophobic treatment of visualization fixture

The contact angle of the acrylic plate surface was hydrophilic. In order to reduce the water flow resistance, it is necessary to change it with hydrophobic treatment. It can be divided into three steps. First, the acrylic sheet with the carved waveform channels was placed in a plasma cleaner (HM-Plasma-MZI, China) in an air atmosphere for 30 min to produce hydroxyl groups on its surface and remove impurities. Then, immersed the acrylic sheet in a 5% octadecyl trichlorosilane solution in a mixture of methanol and toluene for 5 minutes. Finally, dried it at 80°C.

SI-2 Design and optical image of the filtration mold

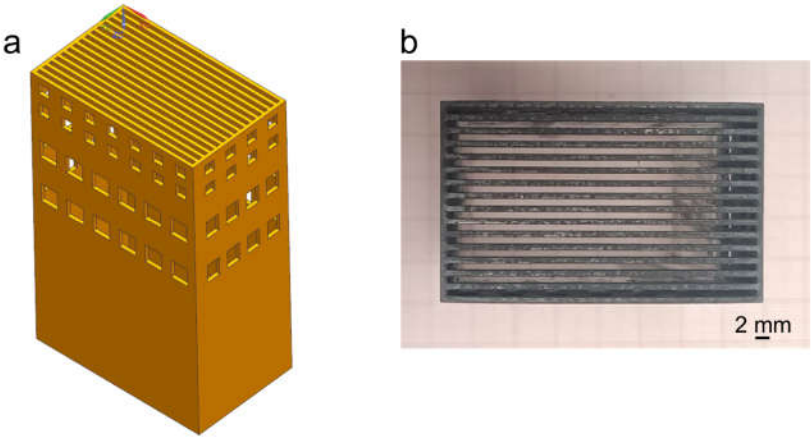

Fig. S1 Design and optical image of the filtration mold. (a) Drawing of the filtration mold. (b) Optical image of the filtration mold by 3D printing.

The mold was designed using the UG software. The rib and space of mold are both 1 mm.

SI-3 Cross-sectional SEM image of three functional layers in 3D-patterned GDL

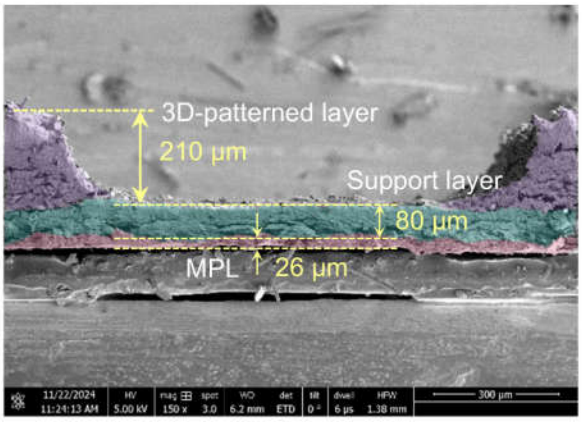

Fig. S2 Cross-sectional SEM image of three functional layers in 3D-patterned GDL.

SI-4 Contact angle tests of three layers in 3D-patterned GDL

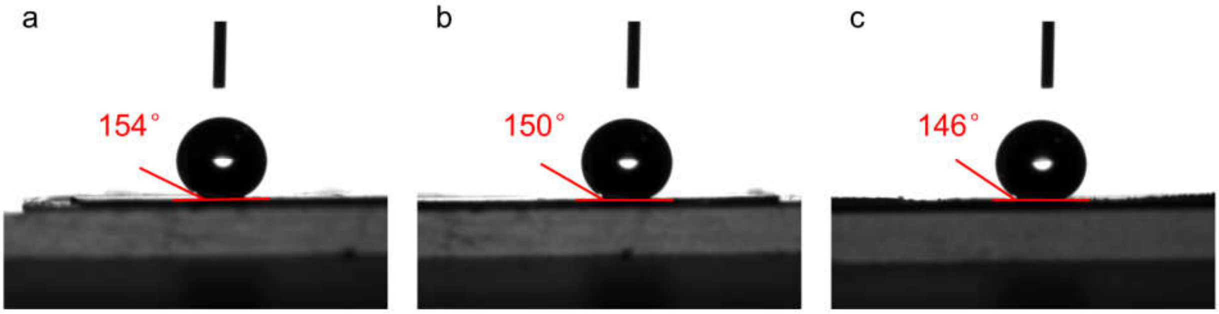

Fig. S3 Contact angle tests of three layers in 3D-patterned GDL. (a) Contact angle of MPL. (b) Contact angle of support layer. (c) Contact angle of 3D-patterned layer.

SI-5 Optical images of conventional waveform and parallel bipolar plates

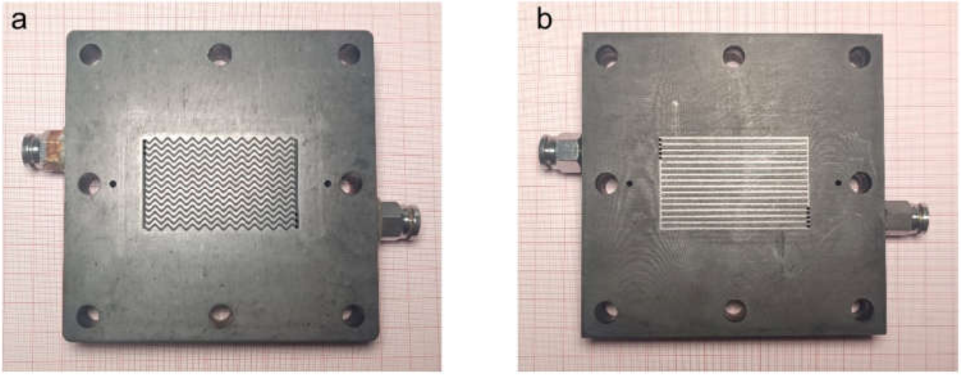

Fig. S4 Optical images of conventional waveform and parallel bipolar plates. (a) Image of the waveform bipolar plate (b) Image of the parallel bipolar plate.

The rib and channel width of conventional waveform and parallel bipolar plates are both 1mm. The active area is 3*5 cm^2.

SI-6 Cross-sectional SEM images of 3D-patterned and conventional GDL

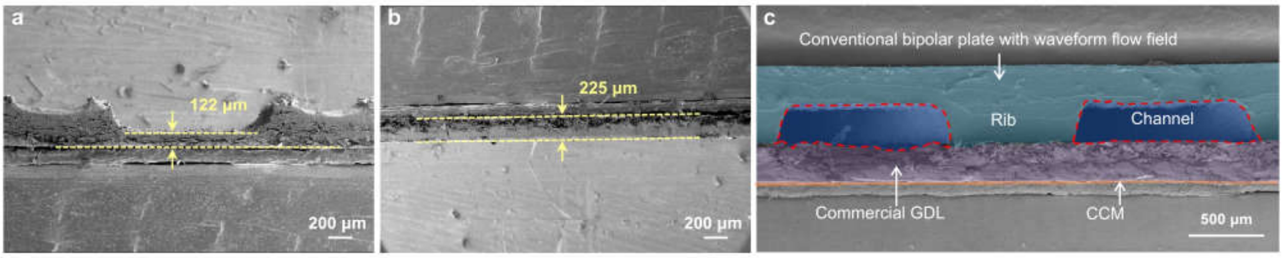

Fig. S5 Comparison of cross-sectional SEM images of 3D-patterned and conventional GDL. (a) 3D-patterned GDL. (b) Conventional GDL. (c) Cross-sectional SEM image of conventional flow field.

The thickness of bottom layer of 3D-patterned GDL after compressed in the fuel cell is about 122 μm (**Fig. S5a**), and the conventional GDL is about 225 μm (**Fig. S5b**), which is much thicker. It would result in the air being able to reach the catalytic layer through a shorter pathway. Consequently, the 3D-patterned GDL could transport air more efficiently.

SI-7 Square resistance of 3D-patterned and conventional GDL

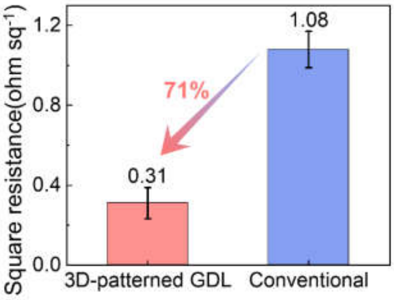

Fig. S6 Square resistance 3D-patterned and conventional GDL.

3D-patterned GDL exhibits a square resistance of 0.31 Ω·sq^{-1}, with a 71% reduction over conventional GDL (1.08 Ω·sq^{-1}), which promotes efficient electron transfer.

SI-8 PEMFC performance of 3D flow field at different air stoichiometric ratios

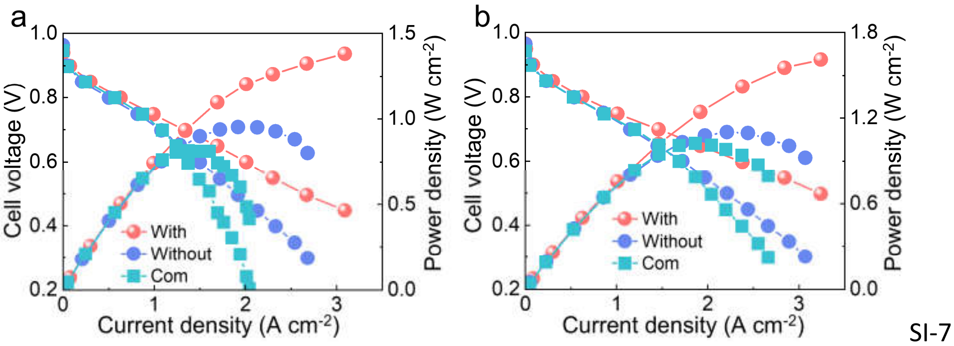

Fig. S7 Fuel cell performance of 3D-patterned GDL, GDL only including MPL and the support layer and the commercial GDL at different air stoichiometric ratios. (a) Polarization curves under 1.5 stoichiometric ratio. (b) Polarization curves under 2.0 stoichiometric ratio.

SI-9 Electrochemical impedance spectroscopy of 3D flow field

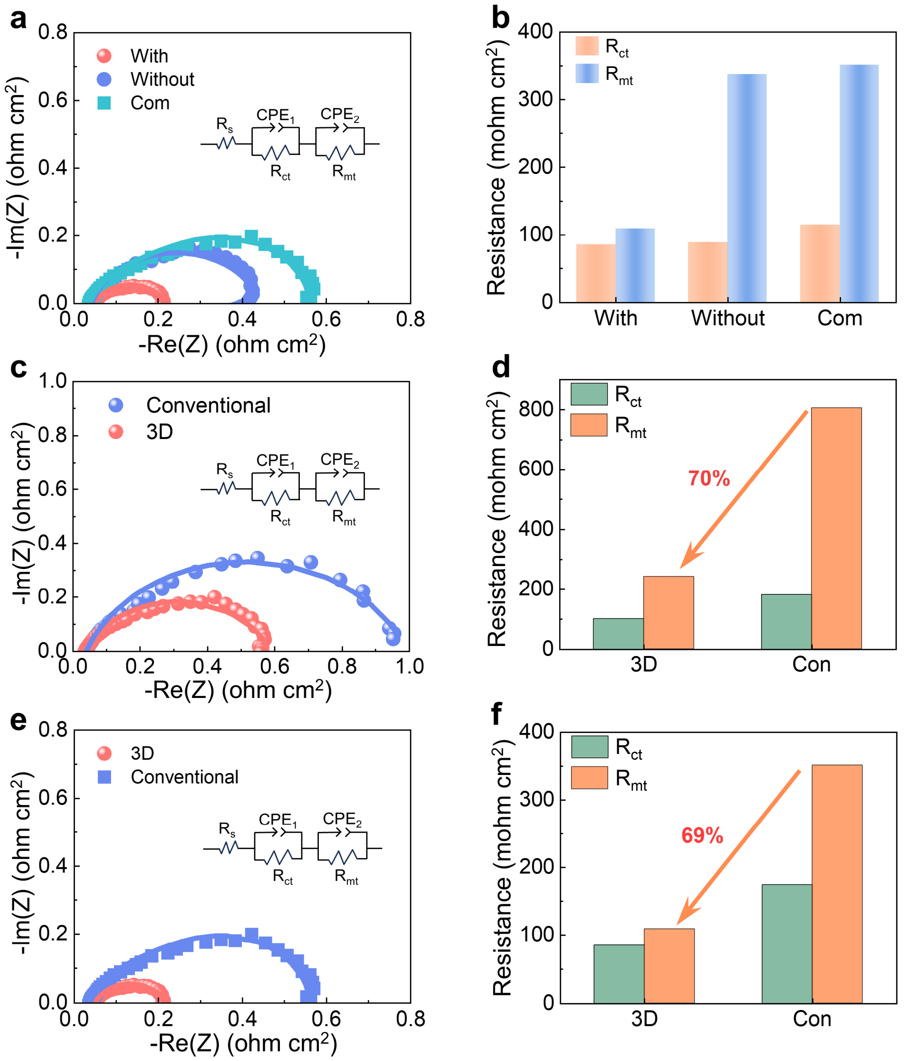

Fig. S8 EIS of PEMFCs. (a) EIS tests of 3D pattern, without 3D pattern and commercial GDL. (b) Fitting results of mass transfer resistance and charge transfer resistance. (c) EIS tests under 1.5 stoichiometric ratio. (d) Fitting results of mass transfer resistance and charge transfer resistance under 1.5 stoichiometric ratio. (e) EIS tests under 2.5 stoichiometric ratio. (f) Fitting results of mass transfer resistance and charge transfer resistance under 2.5 stoichiometric ratio.

SI-10 Comparison of electrochemical active surface area.

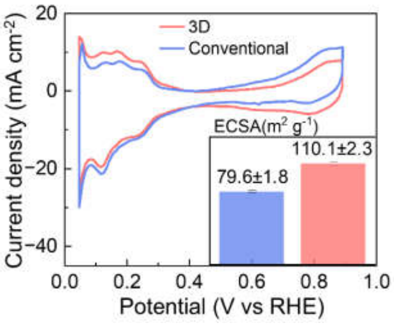

Fig. S9 Electrochemical active surface area of 3D and conventional flow fields.

ECSA of 3D flow field is approximately 38% higher than that of conventional GDL (110.1 ± 2.3 m^2g^{-1} vs. 79.6 ± 1.8 m^2g^{-1}), indicating abundant reactants in the catalyst layer and lower electron transfer impedance.

SI-11 Optimal content of each component of 3D-patterned layer

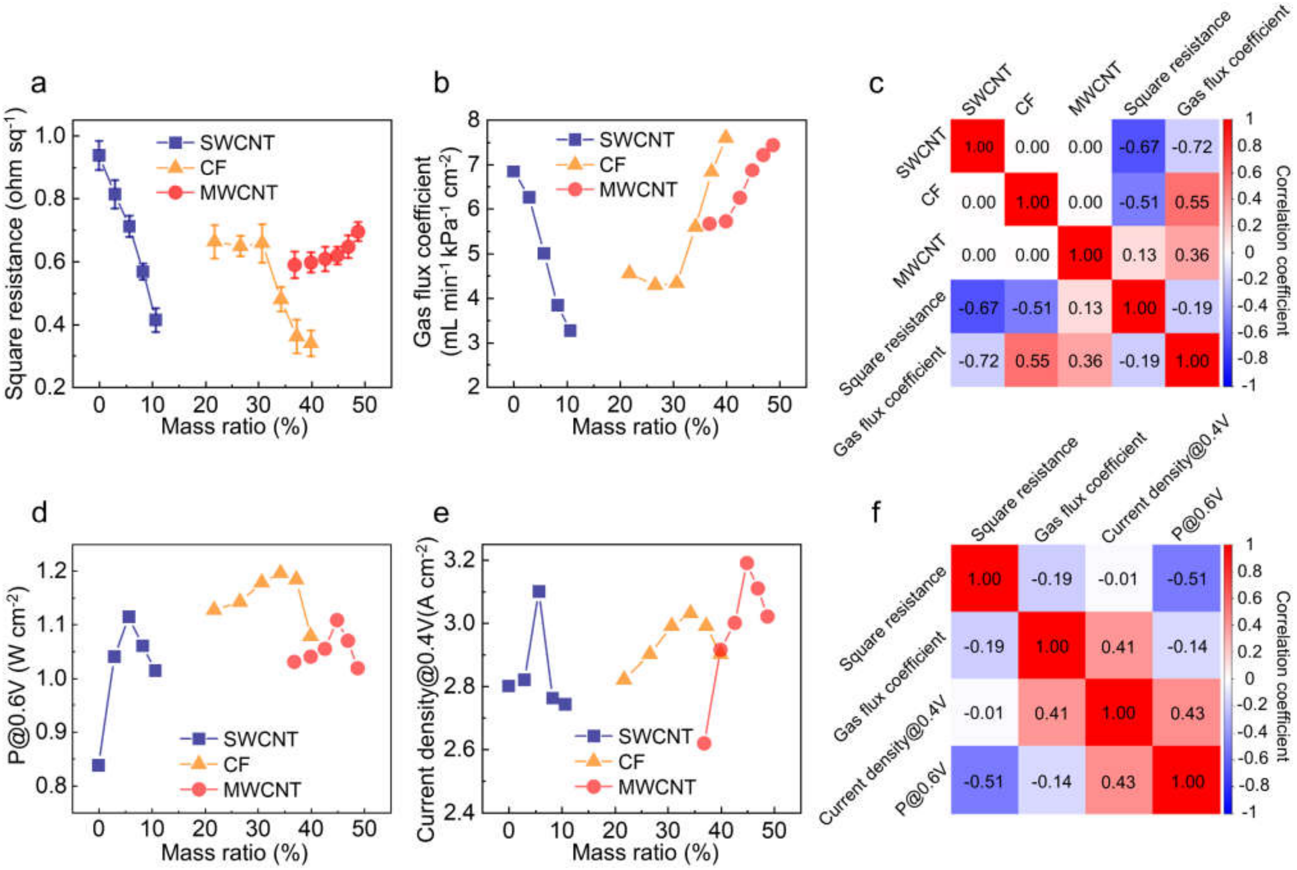

Fig. S10 Effects of SWCNT, CF, and MWCNT with different contents in the 3D-patterned layer. (a) Square resistance. (b) Gas flux coefficient. (c) Analysis of correlation between SWCNT, CF, MWCNT and square resistance, gas flux coefficient. (d) Comparison of power density at 0.6 V with different mass ratios. (e) Comparison of current density at 0.4 V with different mass ratios. (f) Analysis of correlation between square resistance, gas flux coefficient and power density at 0.6 V, current density at 0.4 V.

The 3D-patterned layer of the GDL is composed of SWCNT, MWCNT, CF and PTFE. To investigate the effect of the three carbon materials on the PEMFC performance, we changed the mass ratio of one component at a time, while others keeping constant. According to the existing experience[2, 3], the percentage of PTFE remained unchanged at 20% to maintain a suitable hydrophobicity and porosity.

Firstly, the contents of SWCNTs, CFs, and MWCNTs significantly influence the electron transfer of GDL. As shown in **Fig. S10a**, when mass ratio of SWCNT increases from 0 to 10.7%, the square resistance decreases from 0.938 ohm·sq^{-1} to 0.413 ohm·sq^{-1} (blue points), with a 56% reduction. To comprehensively analyze the effect of components content on the conductivity of GDL, we investigated the correlation between these components and square resistance. As shown in **Fig. S10c**, the correlation coefficient between SWCNT and square resistance is -0.67, indicating a relatively strong negative correlation. This suggests that SWCNT can significantly enhance the conductivity of GDL. When CFs increase from 21.8% to 30.8%, the proportion of CF in the total content is still relatively small. CFs do not fully bridge or contact with each other, resulting in minimal change in square resistance. As CFs continue to increase, the square resistance declines significantly, with an overall reduction of 49% (orange points). The correlation coefficient between CF and square resistance is -0.51, indicating that CF also contributes to the GDL's conductivity. In contrast, as MWCNTs increase, the square resistance shows only a slight upward trend (red points), and the correlation coefficient is 0.13, suggesting a negligible correlation.

Secondly, the variation in the content of SWCNTs, CFs, and MWCNTs influences the gas permeability of GDL. As shown in **Fig. S10b**, more SWCNTs lead to a gradual decrease in the gas flux coefficient. The correlation coefficient is -0.72, indicating a strong negative correlation. It can be attributed to the increased thickness and structural compactness of GDL, which impedes gas penetration. When CFs increases initially, there is minimal effect on the gas permeability. Similarly, it was due to the insufficient contact between the fibers. As CF contents continue to rise, the gas permeability improved significantly, with a correlation coefficient of 0.55. The fibers can interconnect with each other successfully and create large pores in the 3D-patterned layer. MWCNT also has a slight enhancing effect on the gas permeability, showing a weak correlation (Correlation coefficient = 0.36) with the gas flux coefficient. Its loose, multi-layered structure facilitates the formation of micro pores, although the improvement of gas permeability remains limited.

Thirdly, the effect of the three components on fuel cell performance is shown in**Fig. S10d** and **Fig. S10e**. Both of the power density@0.6 V and current density@0.4 V exhibit a volcanic trend with the increasing components mass ratios. The polarization curves at different air stoichiometric ratios of varying SWCNT contents are shown in **Fig. S13**. SWCNT could enhance the electron transfer efficiency of GDL but densify its structure with contents increasing, thereby increasing mass transfer resistance greatly and reducing performance. The role of CF in the GDL primarily involves enhancing conductivity and forming macropores. However, excessive CFs accumulated on the surface of GDL instead of being embedded within, as shown in the cross-sectional SEM images in**Fig. S14**. As a result, they fail to effectively create macropores and increases the contact resistance of GDL instead, leading to the performance decline (**Fig. S16**). The loose and porous structure of MWCNT contributes to the enrichment of porosity within the GDL. As shown in **Fig. S19**, the optimal MWCNT content decreases progressively as the air stoichiometric ratio increases. At low air supply, a more abundant porosity is required for efficient gas transfer. When the stoichiometric ratio increases to 2.5, the adequate gas supply and the macropores created by CFs already ensure sufficient mass transfer. Further increase in MWCNT content contributes negligibly to mass transfer instead, and the greater thickness reduces fuel cell performance meanwhile.

To further investigate the relationship between PEMFCs performances and physical properties of the 3D-patterned GDL, the correlations analysis between power density@0.6 V, current density@0.4 V and square resistance, gas flux coefficient is demonstrated in **Fig. S10f**. First, there is almost no correlation between current density @0.4 V and square resistance. The conductivity of GDL primarily influences electron transfer and barely on the limiting current density. Therefore, a moderate negative correlation is observed with power density@0.6 V (Correlation coefficient = -0.51). Second, power density@0.6 V shows almost no correlation with the gas flux coefficient. Gas permeability primarily has a direct impact on mass transfer efficiency instead of electron transfer. Accordingly, there is a moderate positive correlation (Correlation coefficient = 0.41) between the gas permeability and limiting current density.

SI-12 Cross-sectional SEM images of GDL with different SWCNT contents

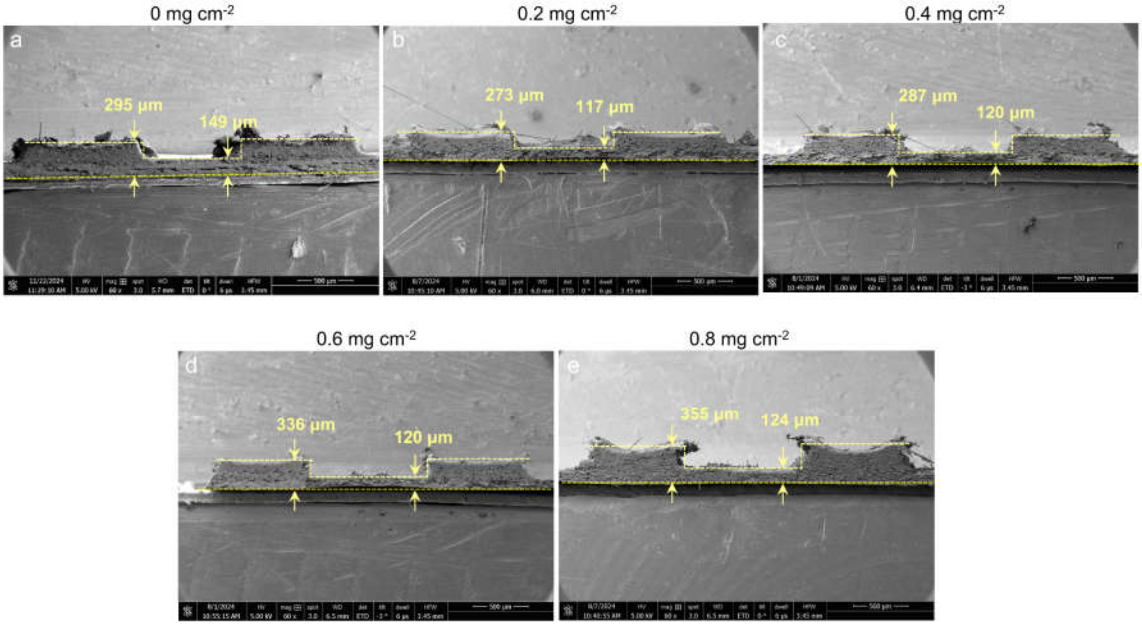

Fig. S11 Cross-sectional SEM images of GDL with different SWCNT contents in the 3D-patterned layer. (a) 0 mg cm^{-2} SWCNT. (b) 0.2 mg cm^{-2} SWCNT. (c) 0.4 mg cm^{-2} SWCNT. (d) 0.6 mg cm^{-2} SWCNT. (e) 0.8 mg cm^{-2} SWCNT.

SI-13 Pressure drops with different SWCNT contents

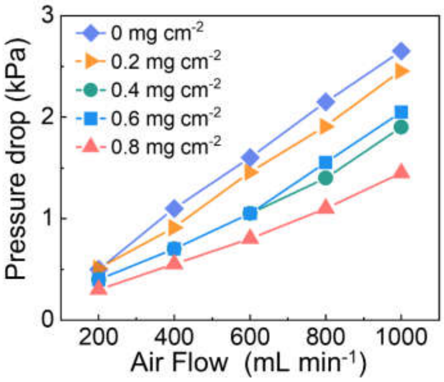

Fig. 12 Pressure drops with different SWCNT contents.

SI-14 Performance with different SWCNT contents at different air conditions

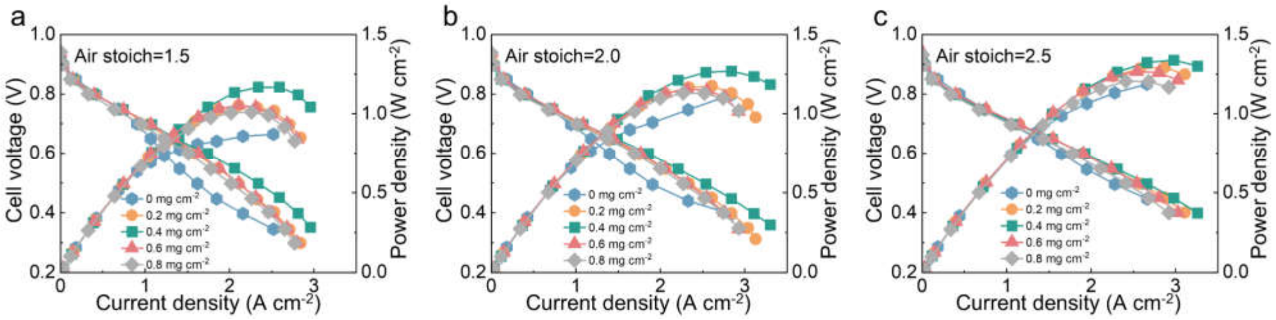

Fig. S13 Fuel cell performance of GDL with different SWCNT contents. (a) Polarization curves under 1.5 stoichiometric ratio. (b) Polarization curves under 2.0 stoichiometric ratio. (c) Polarization curves under 2.5 stoichiometric ratio.

SI-15 Cross-sectional SEM images with different CF contents

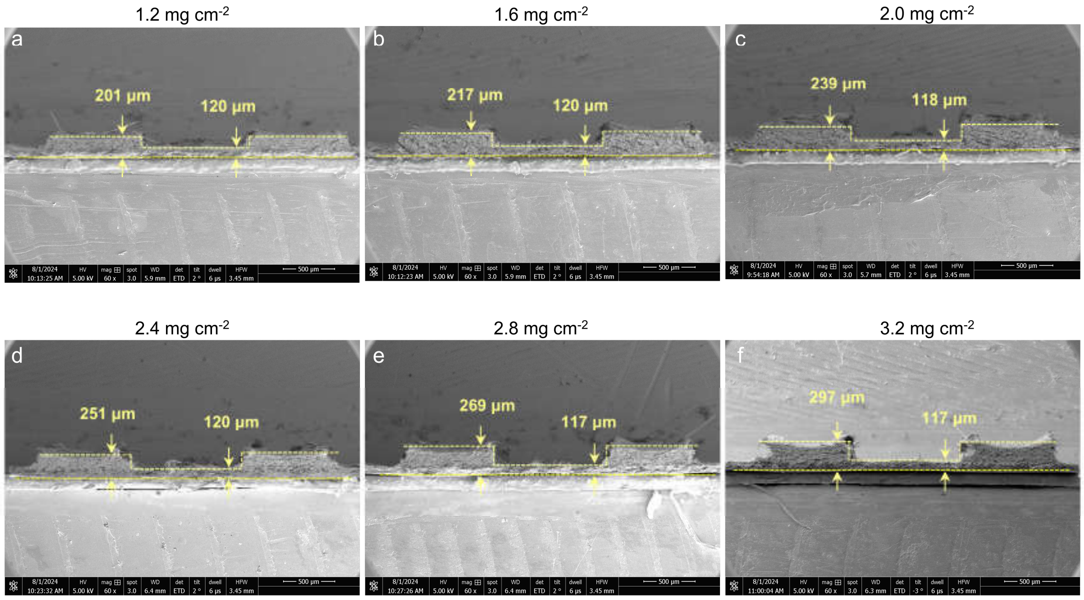

Fig. S14 Cross-sectional SEM images of GDL with different CF contents in the 3D-patterned layer. (a) 1.2 mg cm^{-2} CF. (b) 1.6 mg cm^{-2} CF. (c) 2.0 mg cm^{-2} CF. (d) 2.4 mg cm^{-2} CF. (e) 2.8 mg cm^{-2} CF. (f) 3.2 mg cm^{-2} CF.

SI-16 Pressure drops with different CF contents

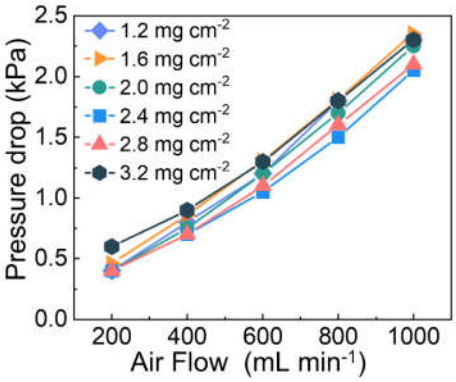

Fig. S15 Pressure drops with different CF contents.

SI-17 Performance with different CF contents under different air conditions

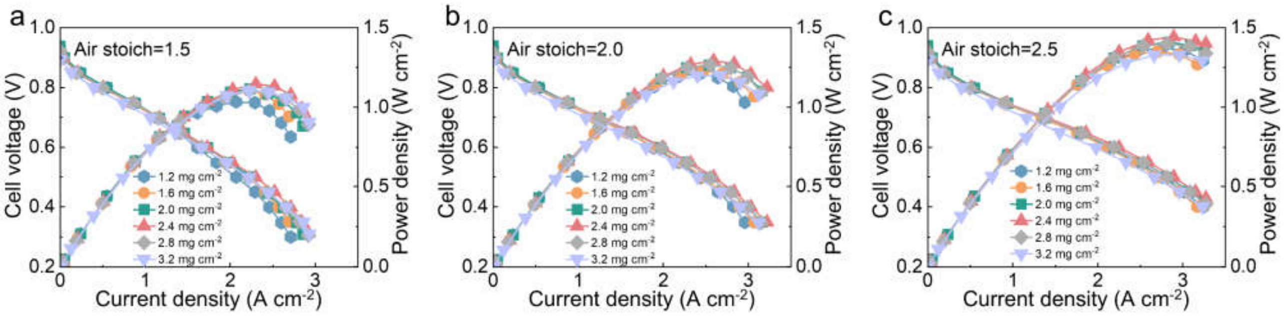

Fig. S16 Fuel cell performance of GDL with different CF contents. (a) Polarization curves under 1.5 stoichiometric ratio. (b) Polarization curves under 2.0 stoichiometric ratio. (c) Polarization curves under 2.5 stoichiometric ratio.

SI-18 Cross-sectional SEM images of GDL with different MWCNT contents

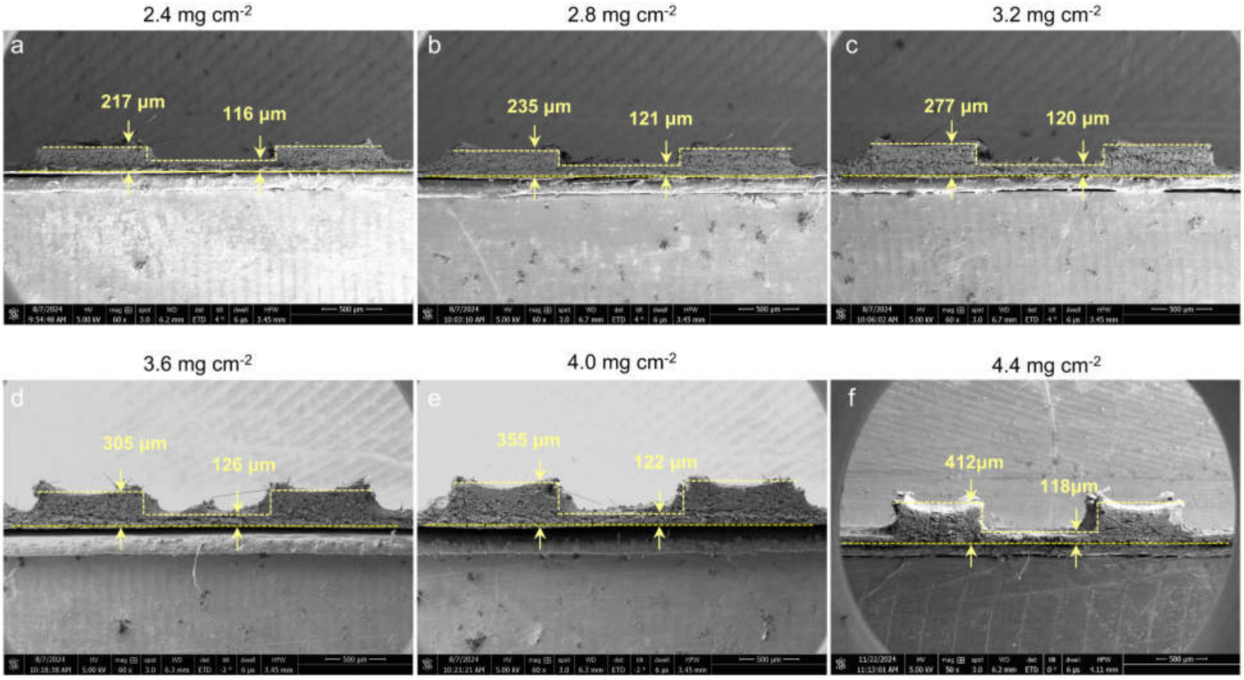

Fig. S17 Cross-sectional SEM image of GDL with different MWCNT contents in the 3D-patterned layer. (a) 2.4 mg cm^{-2} MWCNT. (b) 2.8 mg cm^{-2} MWCNT. (c) 3.2 mg cm^{-2} MWCNT. (d) 3.6 mg cm^{-2} MWCNT. (e) 4.0 mg cm^{-2} MWCNT. (e) 4.4 mg cm^{-2} MWCNT.

SI-19 Pressure drops with different MWCNT contents

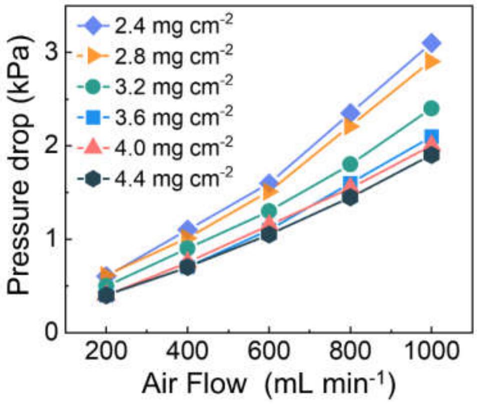

Fig. S18 Pressure drops with different MWCNT contents.

SI-20 Performance with different MWCNT contents at different air conditions

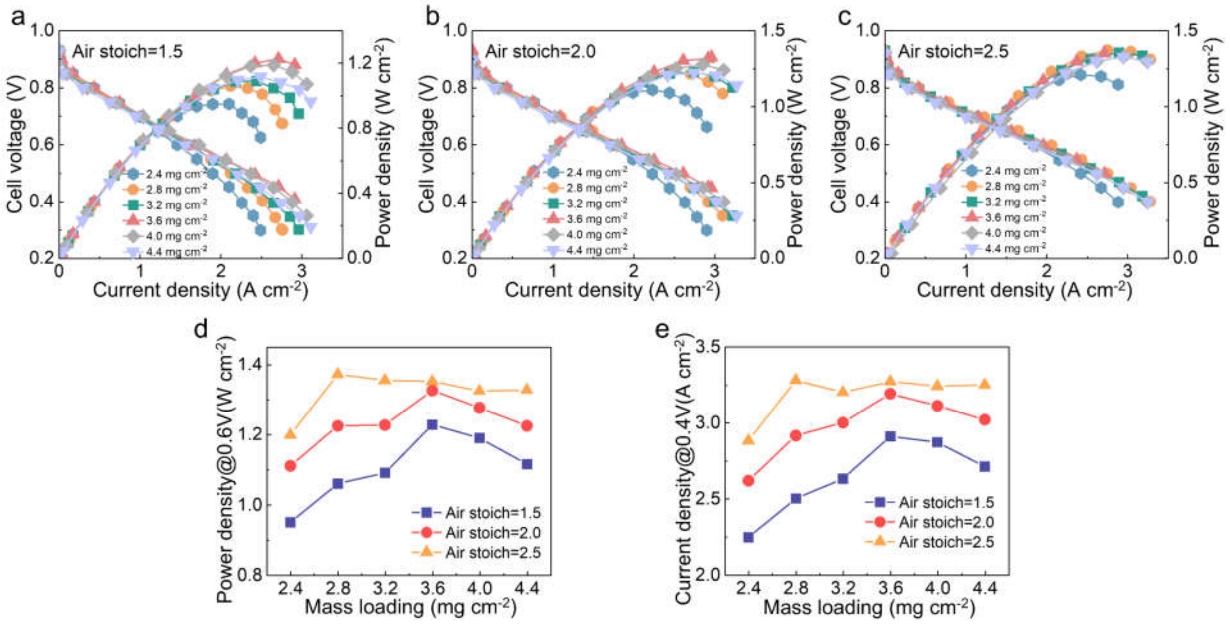

Fig. S19 Fuel cell performance of GDL with different MWCNT contents. (a) Polarization curves under 1.5 stoichiometric ratio. (b) Polarization curves under 2.0 stoichiometric ratio. (c) Polarization curves under 2.5 stoichiometric ratio. (d) Power density at 0.6 V (e) Current density at 0.4 V.

SI-21 Cross-sectional SEM images of GDL with different channel depths

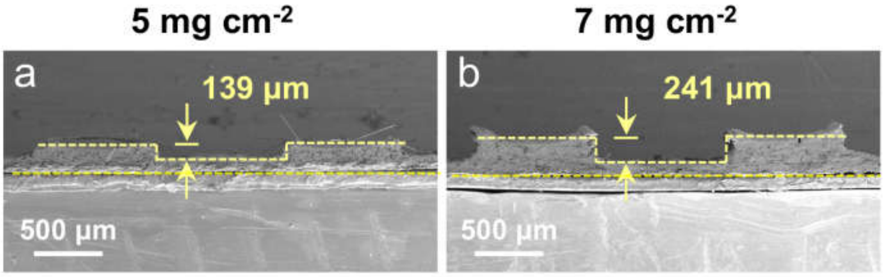

Fig. S20 Cross-sectional SEM images of GDL with different channel depths. (a) Mass loading of 5 mg cm^{-2} in the 3D patterned layer. (b) Mass loading of 7 mg cm^{-2} in the 3D patterned layer.

SI-22 Effect of channel depth on fuel cell performance of 3D flow field

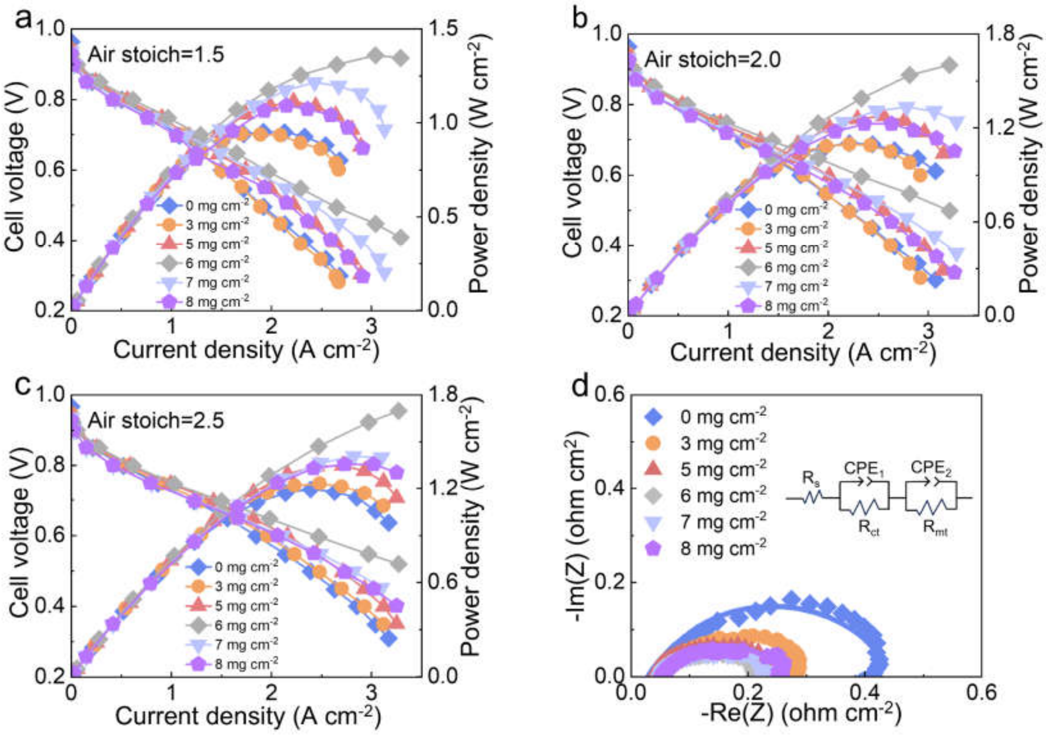

Fig. S21 Fuel cell performance of different channel depths in 3D-patterned GDL. (a) Polarization curves under 1.5 stoichiometric ratio. (b) Polarization curves under 2.0 stoichiometric ratio. (c) Polarization curves under 2.5 stoichiometric ratio. (d) EIS tests under 2.5 stoichiometric ratio.

SI-23 Physical characterization of GDL with different channel depths

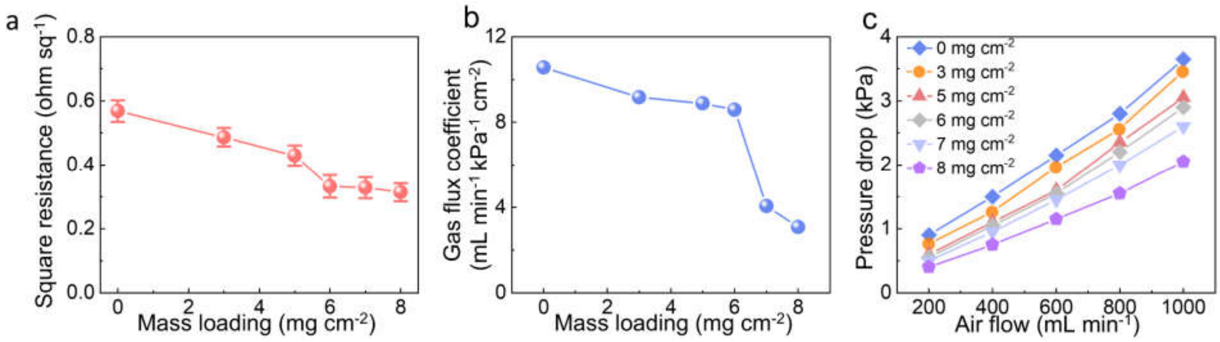

Fig. S22 Physical characterization of 3D-patterned GDL with different channel depths. (a) Square resistance. (b) Gas flux coefficient. (c) Pressure drop.

As shown in **Fig. S22a**, square resistance decreases as the 3D-patterned layer mass loading increased. That's because the 3D-patterned layer is getting higher.[4, 5] At the same time, gas flux coefficient decreases as the 3D-patterned layer height increased, as shown in **Fig. S22b**. When mass loading changes from 0 to 6 mg cm^{-2}, the gas permeability declines slightly. However, there is a plummet when coming to 7 mg cm^{-2}. This indicates that 3D-patterned GDL with much deeper channels is not conducive to gas transfer. Consequently, it has poor mass transfer performance in the fuel cell test. In order to know how the channel depth effected 3D flow field, we test the pressure drop as shown in **Fig. S22c**. The pressure drop declined due to the much more space for gas.

SI-24 Optical images of 3D-patterned GDL with different structures

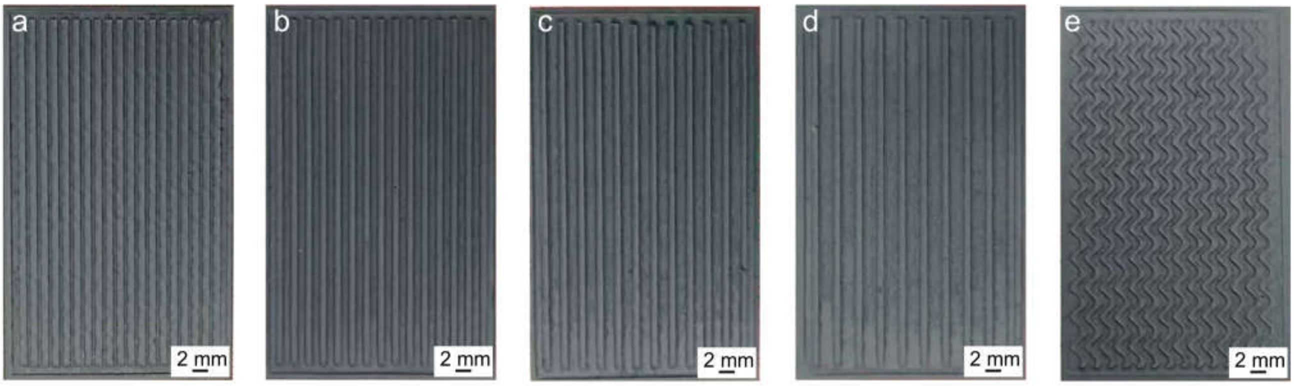

Fig. S23 Optical images of 3D-patterned GDL with different structures. (a) Parallel patterns with 0.5 mm channel. (b) Parallel patterns with 1.0 mm channel. (c) Parallel patterns with 1.5 mm channel. (d) Parallel patterns with 2.0 mm channel. (e) Wavy patterns with 1.0 mm channel.

The channel width is set to 0.5 mm, 1.0 mm, 1.5 mm, and 2.0 mm by adjusting the rib width of the filtration mold. The width of ribs and the depth of channel in the 3D-patterned GDL are kept unchanged. The wavy channel is designed as the waveform with a period of 12, amplitude of 0.8 mm, rib and channel both of 1 mm.

SI-25 Fuel cell performance of 3D flow field with different structures

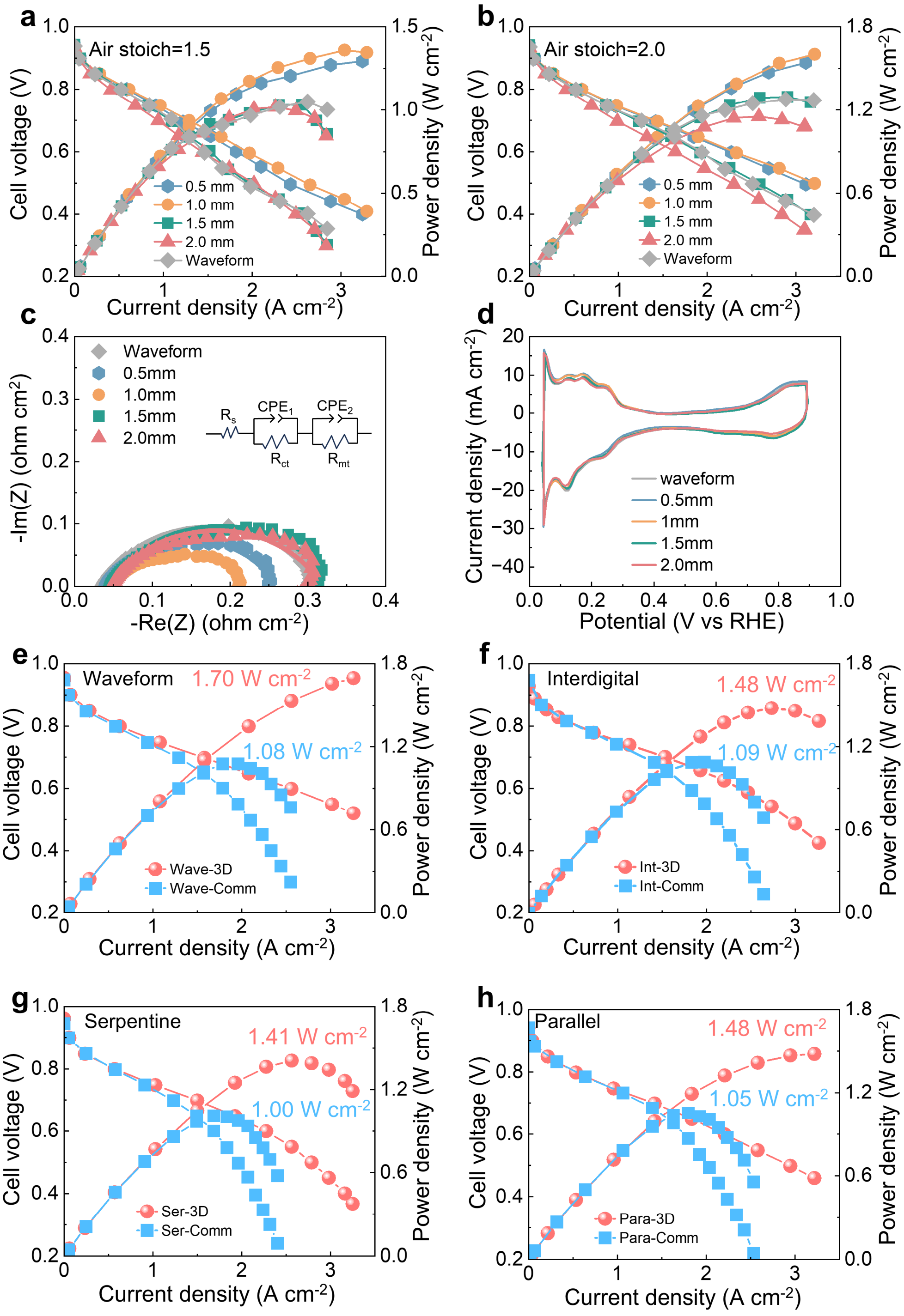

Fig. S24 Fuel cell performance of 3D flow field with different structures. (a) Polarization curves under 1.5 stoichiometric ratio. (b) Polarization curves under 2.0 stoichiometric ratio. (c) EIS tests under 2.5 stoichiometric ratio. (d) LSV curves. Performance of 3D flow fields constructed with different types of bipolar plates. (e) Waveform. (f) Interdigital. (g) Serpentine. (h) Parallel.

SI-26 Effect of MPL mass loading on fuel cell performance

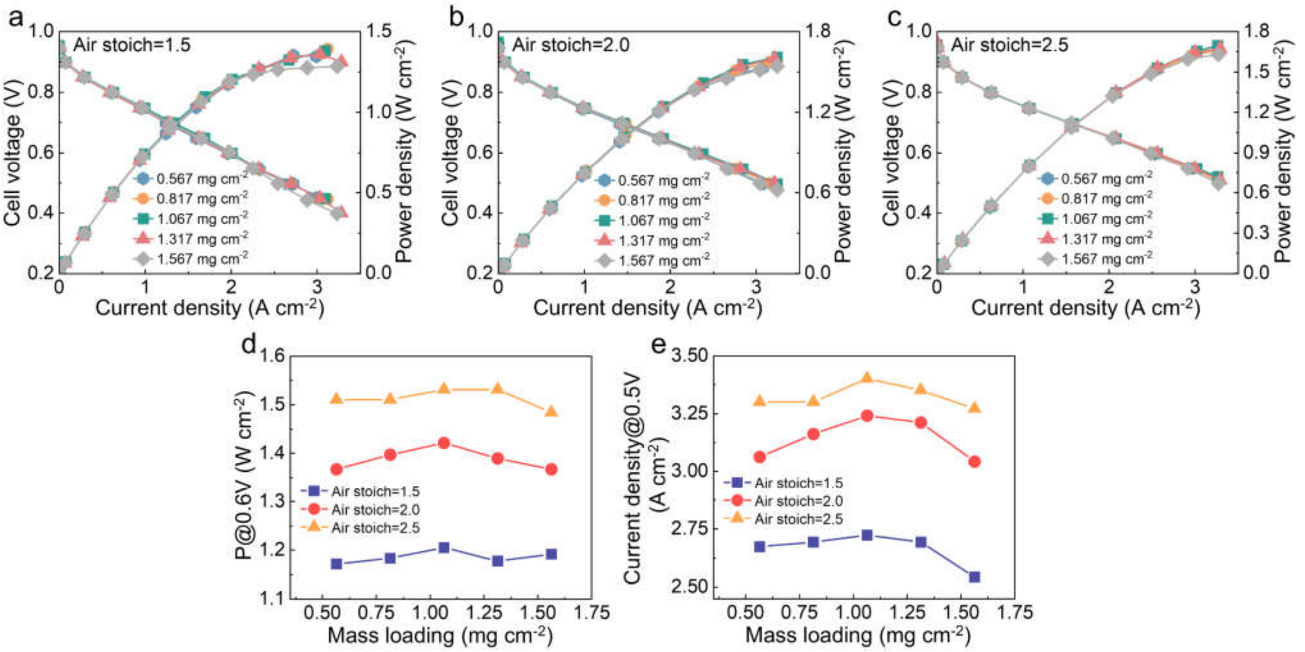

Fig. S25 Effect of MPL mass loading on fuel cell performance. (a) Polarization curves under 1.5 stoichiometric ratio. (b) Polarization curves under 2.0 stoichiometric ratio. (c) Polarization curves under 2.5 stoichiometric ratio. (d) Comparison of power density at 0.6 V under different stoichiometric ratios. (e) Comparison of current density at 0.5 V under different stoichiometric ratios.

In order to get the MPL with optimum thickness for the 3D-patterned GDL, we adjusted a series of mass loading of MPL. As shown in **Fig. S25a-c**, there was no obvious difference between different mass loading through the polarization curves under 1.5, 2.0, and 2.5 stoichiometric ratio. From comparison of power density at 0.6 V and current density at 0.5 V, the MPL mass loading of 1.067 mg cm^{-2} had the best fuel cell performance as shown in **Fig. S25d-e**. The MPL always had the excellent mass transfer ability when mass loading lower than 1.067 mg cm^{-2}. But when came to higher loading, there was obvious performance decline due to the thicker MPL.

SI-27 Effect of support layer mass loading on fuel cell performance

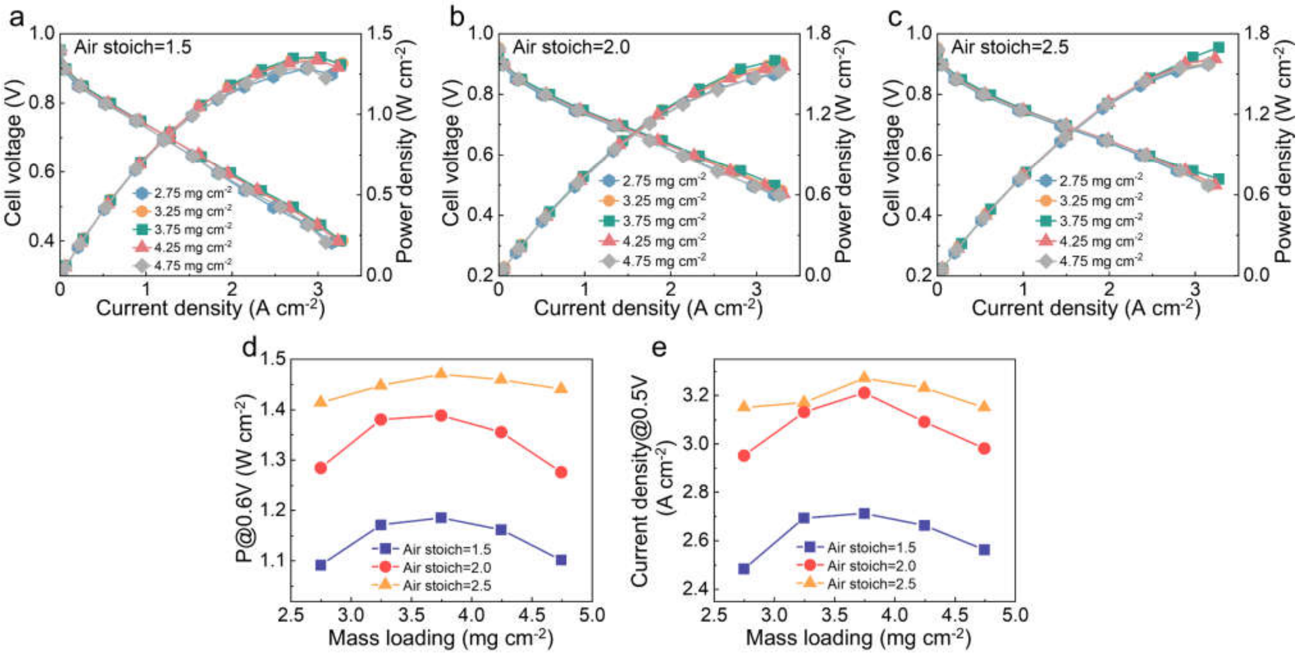

Fig. S26 Effect of support layer mass loading on fuel cell performance. (a) Polarization curves under 1.5 stoichiometric ratio. (b) Polarization curves under 2.0 stoichiometric ratio. (c) Polarization curves under 2.5 stoichiometric ratio. (d) Comparison of power density at 0.6 V under different stoichiometric ratios. (e) Comparison of current density at 0.5 V under different stoichiometric ratios.

In order to get the support layer with optimum thickness for the 3D-patterned GDL, we adjusted a series of mass loading. As shown in **Fig. S26a-c**, there was slight difference between different mass loading through the polarization curves under 1.5, 2.0, and 2.5 stoichiometric ratio. From comparison of power density at 0.6 V and current density at 0.5 V, the MPL mass loading of 3.75 mg cm^{-2} had the best fuel cell performance as shown in **Fig. S26d-e**. When mass loading lower than 3.75 mg cm^{-2}, the support layer failed to provide sufficient transition and support between MPL and 3D-patterned layer. And when mass loading higher than 3.75 mg cm^{-2}, the mass transfer performance decreased due to the thicker support layer.

SI-28 Fuel cell performance of conventional flow field under different humidity

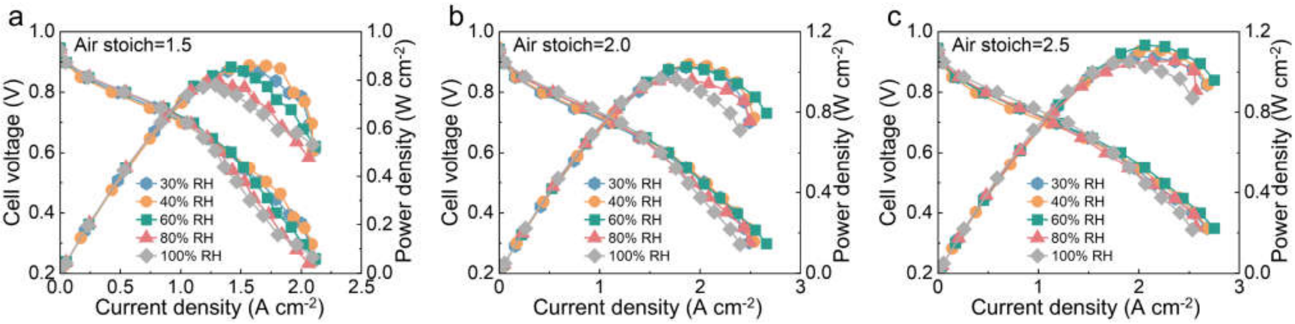

Fig. S27 Fuel cell performance of conventional flow field under different relative humidity. (a) Polarization curves under 1.5 stoichiometric ratio. (b) Polarization curves under 2.0 stoichiometric ratio. (c) Polarization curves under 2.5 stoichiometric ratio.

SI-29 Fuel cell performance of 3D flow field under different relative humidity

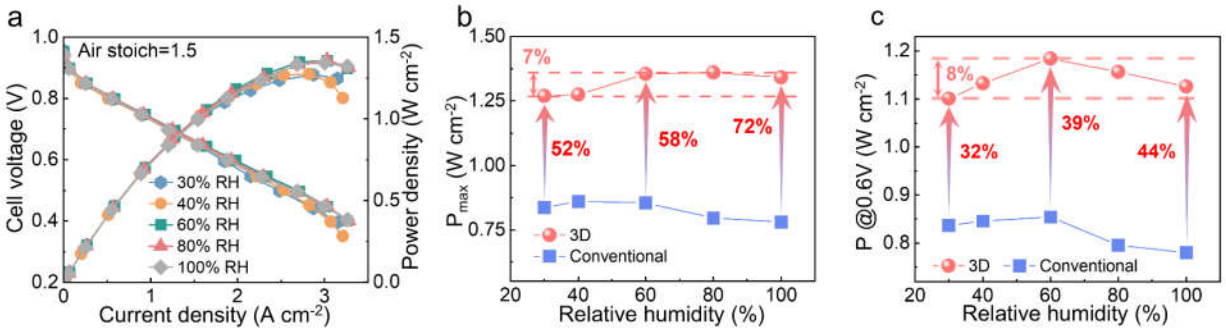

Fig. S28 Fuel cell performance of 3D flow field under different relative humidity. (a) Polarization curves under 1.5 stoichiometric ratio. (b) Comparison of peak power density under different relative humidity. (c) Comparison of power density at 0.6 V under different relative humidity.

SI-30 Performance of conventional flow field under different back pressures

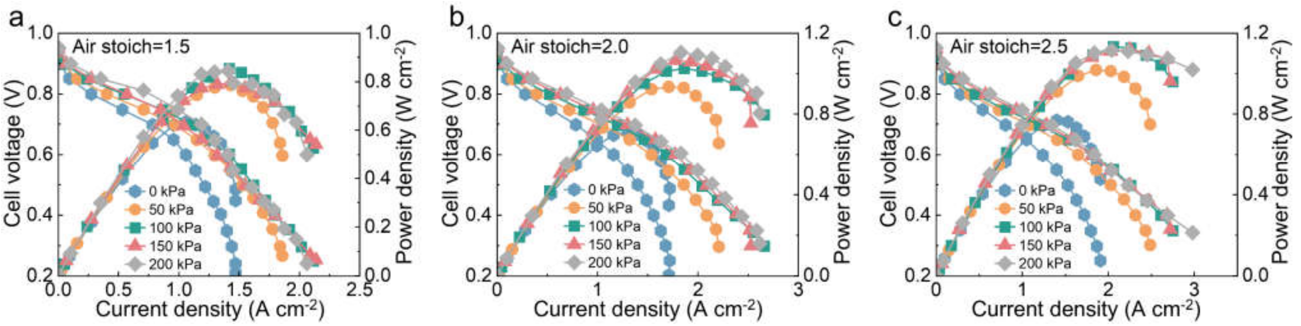

Fig. S29 Fuel cell performance of conventional flow field under different back pressures. (a) Polarization curves under 1.5 stoichiometric ratio. (b) Polarization curves under 2.0 stoichiometric ratio. (c) Polarization curves under 2.5 stoichiometric ratio.

SI-31 Fuel cell performance of 3D flow field under different back pressures

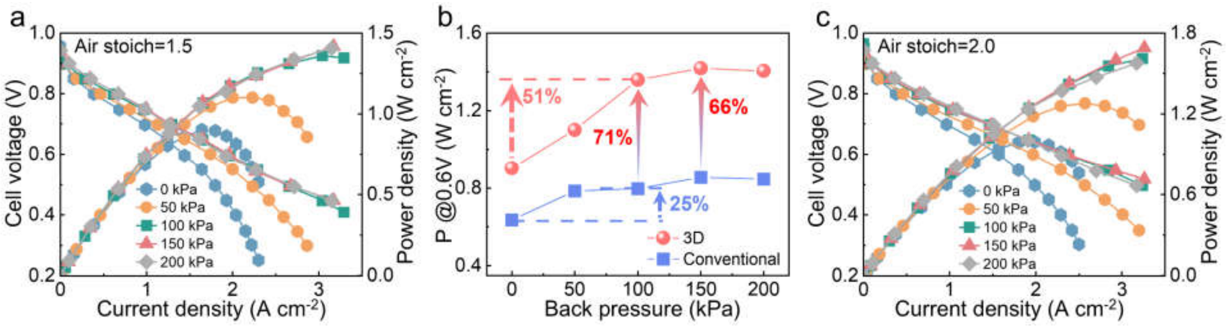

Fig. S30 Fuel cell performance of 3D flow field under different back pressures. (a) Polarization curves under 1.5 stoichiometric ratio. (b) Comparison of power density at 0.6 V under different back pressures. (c) Polarization curves under 2.0 stoichiometric ratio.

SI-32 Optical images of the visualization fixture

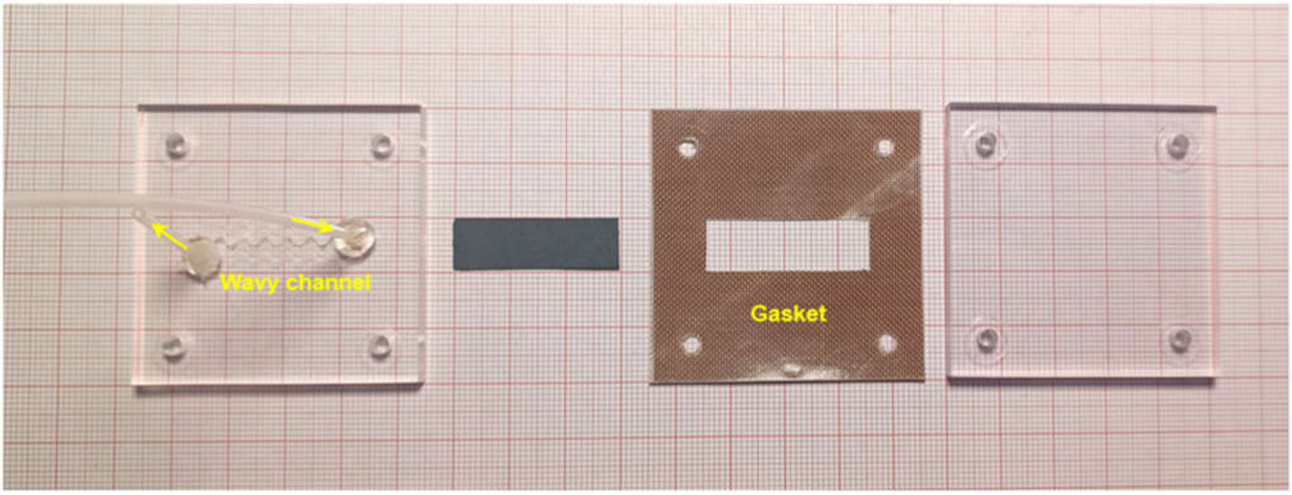

Fig. S31 Optical images of the visualization fixture.

To replicate the flow field environment in the fuel cell accurately, the shape, channel depth (300 μm), channel width (1 mm), and rib width (1 mm) of the engraved flow channels on the acrylic plates keep identical to those of conventional waveform bipolar plate.

SI-33 Water production in the fuel cells

Current density	Water production in 60 s
3 A cm^{-2}	40.29 mg
3.5 A cm^{-2}	47.01 mg
4.0 A cm^{-2}	53.7 mg

Table S1 Water production in 60 s under high current density.

In order to simulate the water during the fuel operating status more accurately, we calculated water production at different high current densities.[6, 7] We assumed that all water produced is liquid for easier observation. We subsequently calculated the water production in the fuel cell at high current density to determine the volume of liquid water injected into the fixture. The effective area of the visualization fixture is 0.8 cm*3 cm. Water production is listed in **Table S1** within 60 seconds at 3 A cm^{-2}, 3.5 A cm^{-2}, and 4.0 A cm^{-2}, which are 40.3 mg, 47.0 mg, and 53.7 mg, respectively. During fuel tests under different air stoichiometric ratios in the 3 cm × 5 cm single cell, the minimum air flow rate to the cathode was set to 500 mL min^{-1}. Correspondingly, the minimum air flow rate in the visualization fixture is 80 mL min^{-1} adjusted for the change in effective area. Consequently, we determined the air flow rates in the visualization fixture: 80 mL min^{-1}, 120 mL min^{-1}, 160 mL min^{-1}, and 200 mL min^{-1}, corresponding to 1, 1.5, 2.0, and 2.5 times of the minimum air flow rate, respectively.

SI-34 Contact angles of fixture surface before and after hydrophobic treatment

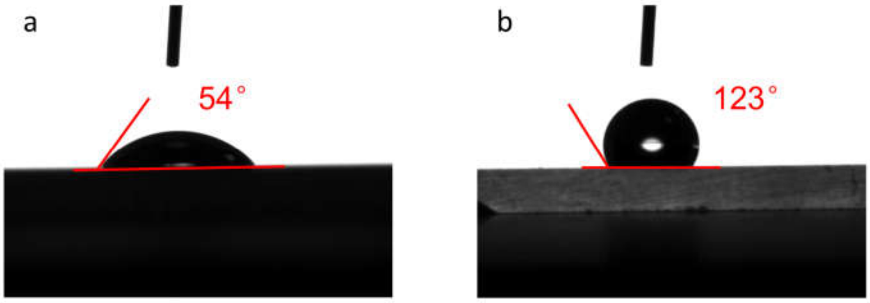

Fig. S32 Contact angles of fixture surface before and after hydrophobic treatment. (a) The plate surface before hydrophobic treatment. (b) The plate surface after hydrophobic treatment.

After the treatment, the contact angle of its surface had changed from 54° to 123°, transforming it from hydrophilic state to the hydrophobic state successfully.

SI-35 Videos of water behavior recorded in the flow field

In addition, we also observed water removal under varying water production and air flow rates. Firstly, with a fixed water injection of 50 μL, the water behavior in the flow field under low air flow rate of 80 mL min^{-1}, is demonstrated in **Video S3**. In the 3D flow field, there is also efficient water removal through cross-channel transfer. Secondly, we adjusted the water injection to 90 μL under 120 mL min^{-1} air flow rate. **Video S4** demonstrate the robust capacity to expel substantial amounts of liquid water of 3D flow field. Consequently, the 3D flow field exhibits excellent water flooding resistance due to the shortest water flow pathway, without being confined to the flow channels under any air flow rate and liquid water volume.

Video S1, **Video** S3 and **Video S4** are played at 0.1 times of speed. **Video S2** is played at the original speed.

SI-36 References

1 X. Fu, J. Wei, F. Ning, C. Bai, Q. Wen, H. Jin, Y. Li, S. Zou, S. Pan, J. Chen, S. Deng and X. Zhou, *J. Power Sources*, 2022, **520**, 23082.

2 X. Fu, Q. Wen, J. Han, J. Wei, Y. Li, F. Ning and X. Zhou, *Int. J. Hydrogen Energy*, 2022, **47**, 25769-25779.

3 C. He, Q. Wen, F. Ning, M. Shen, L. He, B. Tian, W. Li, L. Xu, Y. Liu, X. Dan, Z. Chai, S. Zou and X. Zhou, *Adv. Funct. Mater.*, 2024, **34**, 2401261.

4 I.-C. Gau, Y.-W. Chang, G.-S. Chen, Y.-L. Cheng and J.-S. Fang, *Solid State Electron.*, 2024, **215**.

5 G. Feng, Z. Pan, C. Wang, N. Li, Y. Shi, Y. Yan, X. Lu and Y. Xu, *J. Alloys Compd.*, 2024, **1004**, 175936.

6 Q. Wen, S. Pan, Y. Li, C. Bai, M. Shen, H. Jin, F. Ning, X. Fu and X. Zhou, *ACS Energy Lett.*, 2022, **7**, 3900-3909.

7 C. He, Q. Wen, F. Ning, M. Shen, L. He, Y. Li, B. Tian, S. Pan, X. Dan, W. Li, P. Xu, Y. Liu, Z. Chai, Y. Zhang, W. Liu and X. Zhou, *Adv. Sci.*, 2023, **10**, 2302928.